VIII International Conference on Fracture Mechanics of Concrete and Concrete Structures
FraMCoS-8
J.G.M. Van Mier, G. Ruiz, C. Andrade, R.C. Yu and X.X. Zhang (Eds)

NUMERICAL MODELING OF CRYSTALLIZATION-INDUCED DAMAGE

H. DERLUYN[*,†]**, P. MOONEN**[*,†] **AND J. CARMELIET**[*,†]

[*]ETH Zürich, Chair of Building Physics
Wolfgang-Pauli-Strasse 15, 8093 Zürich, Switzerland
e-mail: derluyn@arch.ethz.ch, moonen@arch.ethz.ch, carmeliet@arch.ethz.ch

[†]EMPA, Swiss Federal Laboratories for Materials Science and Technology,
Laboratory for Building Science and Technology
Überlandstrasse 129, 8600 Dübendorf, Switzerland
e-mail: hannelore.derluyn@empa.ch, peter.moonen@empa.ch, jan.carmeliet@empa.ch

Key words: Salt Transport, Crystallization, Salt Damage, Durability, Quasi-Brittle Materials

Abstract. This paper presents a finite element model coupling heat, water and salt transport, salt crystallization, deformation and damage in porous materials. The model allows to predict mechanical, hygro-thermal and crystallization induced damage. The model performance is illustrated by simulating the damage caused by sodium chloride crystallization in Savonnières limestone, a qausi-brittle porous material. The simulation results suggest that we need to control the nucleation and growth kinetics in porous materials to be able to control salt damage.

1 INTRODUCTION

Water and dissolved salt ions penetrate into building materials due to diffusive and advective transport. Upon changes in the environmental conditions, salt can crystallize at the surface (efflorescence) or inside the material (subflorescence). Subflorescence is accompanied with the development of crystallization pressures, which may lead to spalling and cracking of the solid material matrix, and thus to a reduction of the lifetime of a construction or monument. Until now, the mechanism of crystallization in confined conditions and the related damage processes, as well as the computational modeling, are still subject of scientific debate.

Moonen et al. [1–4] developed a FEM model that predicts hygrothermal damage processes in porous media using a continuous-discontinuous approach. This model has been extended by Derluyn [5] to incorporate salt transport, salt crystallization and crystallization damage. The model includes all salt properties of sodium chloride and sodium sulfate, two of the most damaging salts for porous materials. In the first part of this paper, we present the fully coupled model. We briefly recall the modeling of heat and moisture transport [6]. The description of the salt crystallization, the coupling with the mechanical behavior and the crystallization damage are discussed. In the second part of this paper, a simulation study is presented, predicting the damage caused by sodium chloride crystallization induced by drying of an initially wet limestone. The simulation results are compared with experimental data acquired by neutron radiography and X-ray tomography [5].

2 A COUPLED MODEL FOR TRANSPORT, CRYSTALLIZATION, DEFORMATION AND DAMAGE

2.1 Moisture and heat transport

The moisture transport comprises the transport of liquid and water vapor in the pore space, with the liquid phase consisting of water and

salt ions. Exchange of water molecules occurs between the liquid and the gas phase and the liquid and the crystal phase. Salt ions are exchanged between the liquid and the crystal phase. The moisture mass balance is given by:

$$\Phi \frac{\partial \left(S_l \rho_l + S_{cr} \rho_{cr}\right)}{\partial t} = \nabla \cdot \left(\mathbf{K}_l \nabla p_c + \boldsymbol{\delta}_v \nabla p_v\right) \tag{1}$$

with Φ the total accessible porosity, S_l and S_{cr} the liquid and the crystal saturation degree, and ρ_l and ρ_{cr} the density of the liquid phase and of the salt crystal. $\mathbf{K}_l$ is the liquid permeability as function of capillary pressure. The capillary pressure expresses the pressure difference across the liquid-gas interface and is defined as:

$$p_c = p_l - p_g \tag{2}$$

$\boldsymbol{\delta}_v$ is the vapor permeability in function of vapor pressure p_v. The vapor pressure is function of the capillary pressure p_c, temperature T and the water activity a_w as given by the modified Kelvin relation:

$$p_v = a_w p_{v,sat} \exp\left(\frac{p_c}{\rho_w R_v T}\right) \tag{3}$$

with $p_{v,sat}$ the saturated vapor pressure, which is function of the temperature, and ρ_w the water density. The water activity is dependent on the temperature and the salt concentration and accounts for the change of the vapor pressure in equilibrium with a salt solution, compared to the vapor pressure in equilibrium with pure water. For pure water, the water activity equals 1. The higher the salt concentration gets, the lower the water activity will be, leading to lower vapor pressures.

Under the assumption that the dissolved salt ions are transported together, the mass balance for the salt ions reads:

$$\Phi \frac{\partial \left(S_l \rho_l C_i\right)}{\partial t} + \Phi \frac{\partial S_{cr} / \bar{V}_{cr}}{\partial t} = \nabla \cdot \left(\rho_l \mathbf{D}_i^l \nabla C_i\right) + \nabla \cdot \left(C_i \mathbf{K}_l \nabla p_c\right) \tag{4}$$

with C_i the salt concentration in mole/kg liquid solution and $\bar{V}_{cr}$ the molar volume of the salt crystal. $\mathbf{D}_i^l$ is the salt diffusion coefficient in the liquid phase.

Heat transport is described by the energy balance:

$$\frac{\partial \left(\begin{pmatrix} c_{p,s}\rho_s + \Phi c_{p,l} S_l \rho_l + \\ \Phi c_{p,cr} S_{cr} \rho_{cr} \end{pmatrix} \left(T - T_0\right) \right)}{\partial t} + \frac{\partial \Phi L_{cr} S_{cr} \rho_{cr}}{\partial t} + \nabla \cdot \mathbf{q}_e = 0 \tag{5}$$

with $c_{p,j}$ the specific heat capacity at atmospheric pressure of the considered phase ($_s$, solid phase; $_l$, liquid phase; $_{cr}$, crystal phase). L_{cr} is the heat of crystallization and T_0 is the reference temperature for the enthalpy, being 0°C (273.15K).

The heat flux $\mathbf{q}_e$ is a combination of a conductive part and an advective part. The conductive part is given by Fourier's law:

$$\mathbf{q}_{e,c} = -\boldsymbol{\lambda} \nabla T \tag{6}$$

with $\boldsymbol{\lambda}$ the apparent thermal conductivity of the porous structure. The advective part is described as:

$$\mathbf{q}_{e,a} = -\left(c_{p,v}\left(T - T_0\right) + L_v\right) \boldsymbol{\delta}_v \nabla p_v - c_{p,l}\left(T - T_0\right) \mathbf{K}_l \nabla p_c \tag{7}$$

with $c_{p,v}$ the specific heat capacity of water vapor and L_v the latent heat of evaporation of water.

2.2 Salt crystallization

The salt crystal mass balance reads:

$$\Phi \frac{\partial \left(S_{cr} \rho_{cr}\right)}{\partial t} = e_{crl} \tag{8}$$

where we have to define the mass exchange e_{crl} between the liquid and the crystal phase. This mass exchange is described by the kinetics of salt crystallization/dissolution. In brief, the model considers that the supersaturation U is the driving force for crystallization, and consequently the mass exchange during crystallization from a solution is given by [7, 8]:

$$e_{crl} = \zeta K_{m,cr} (U - 1)^{g_{cr}} \text{ for } U > U_{thr} \tag{9}$$

where $K_{m,cr}$ and g_{cr} are kinetic parameters and ζ is the fraction of the capillary active pore space

filled with salt solution. In order for new crystals to nucleate and grow, the supersaturation has to exceed a threshold value U_{thr}.

Dissolution is described by a similar type of equation, only the kinetic parameters and the threshold value differ:

$$e_{crl} = -\zeta K_{m,diss}(1-U)^{g_{diss}} \text{ for } U < 1 \quad (10)$$

For the modeling of the crystallization, besides the kinetics, also the confined pore volume space needs to be considered. If no space is available for crystals to grow, crystallization will stop and consequently the concentration will remain higher than when the crystals could grow freely. Moreover, dissolution can only occur as long as there are still crystals present. Finally, we also have to consider that the presence of crystals at a certain location influences nucleation and growth of crystals at neighboring locations. In order to get a stable numerical system incorporating all these conditions, the crystallization term e_{crl} is implemented as:

$$\begin{aligned} &e_{crl} = \\ &f\left(S_{cr},1\right)\cdot\zeta K_{m,cr}(\max\left(U,U_{thr}\right)-U_{thr})^{g_{cr}}+ \\ &f\left(S_{cr},0\right)\cdot\zeta K_{m,diss}(1-\min\left(U,1\right))^{g_{diss}} \end{aligned} \quad (11)$$

where the first term represents crystal growth and the second term represents crystal dissolution.

The function f is introduced to perform two checks:

1. Crystallization stops when the available pore volume is occupied by salt crystals: as long as $S_{cr} < 1$, f equals 1 and the crystallization kinetics are active. When the pore volume is filled with crystals, $S_{cr} = 1$, no crystallization occurs anymore and consequently f equals 0.
2. Dissolution can occur as long as there are still crystals present: as long as $S_{cr} > 0$, f equals 1. When all crystals are dissolved and $S_{cr} = 0$, the dissolution kinetics stop and f equals 0.

Physically, we would only need a step function to define f, where f equals 1 when $0 < S_{cr} < 1$ and f equals 0 when $S_{cr} = 0$ or $S_{cr} = 1$. However, as step functions typically introduce numerical problems due to their steep change, we smooth the function f by use of an exponential function. The function f is defined as:

$$f\left(x,r\right) = \frac{r-x}{|r-x|}\cdot\left(1-\exp\left(-\left|\frac{x-r}{HBW}\right|\right)\right) \quad (12)$$

The half-band-with HBW of this function is taken low (HBW=0.01) in order to assure that the exponential function reduces fast to 0 and that the function f approximates as close as possible a step function.

The function U_{thr} is defined as:

$$U_{thr} = 1 + (U_{start}-1)\cdot\exp\left(-\upsilon\bar{S}_{cr}\right) \quad (13)$$

and represents the drop of the crystallization threshold from U_{start} to 1. This drop is related to the nucleation and growth kinetics. The nucleation and growth kinetics determine how long a certain supersaturation U is maintained until a sufficient amount of crystals have nucleated and sufficiently large crystals have grown so that new crystals start to grow at lower supersaturation levels. This is incorporated in the parameter υ and the function $\bar{S}_{cr}$. The function $\bar{S}_{cr}$ also incorporates how the crystal growth propagates through the studied domain when a crystal starts to grow locally. A non-local formulation is developed for this function in order to be able to include this propagation. $\bar{S}_{cr}$ is defined as:

$$\bar{S}_{cr} = \frac{\int_\Omega w_f S_{cr}\mathrm{d}\Omega}{\int_\Omega w_f \mathrm{d}\Omega} \quad (14)$$

with w_f the weighting function, defined as a multivariate normal distribution:

$$w_f = \frac{1}{(2\pi)^{\frac{k}{2}}\, l^k}\exp\left(-\frac{r^2}{2l^2}\right) \quad (15)$$

with r the distance away from the evaluated point and l the influence length. k represents the number of dimensions. The influence length depends on the nucleation kinetics. If a lot of crystals nucleate, the influence length will be large, if the number of nucleating crystals is limited, the influence length will be reduced. When no crystals are present in the neighborhood of the evaluated point, $\bar{S}_{cr}$ equals zero

and the U_{thr}-condition remains U_{start}. When many crystals nucleate and grow in the neighborhood, the U_{thr}-condition reduces to one, ensuring that crystals also start to grow in the positions around a position where crystals are already precipitating.

2.3 Conservation of momentum

The solid momentum balance reads:

$$\nabla \cdot \boldsymbol{\sigma}_s + \Phi_s \rho_s \boldsymbol{b}_s = 0 \tag{16}$$

with $\boldsymbol{\sigma}_s$ the partial stress tensor of the solid phase and $\boldsymbol{b}_s$ the body forces working on the solid (for example the gravitational force). For the application of our model, body forces are negligible.

The partial stress tensor of the solid phase is expressed as:

$$\boldsymbol{\sigma}_s = \boldsymbol{\sigma} - b p_s \mathbf{I} \tag{17}$$

with b the Biot coefficient, p_s the solid pressure, $\mathbf{I}$ the second order unit tensor and $\boldsymbol{\sigma}$ the effective stress tensor. p_s accounts for the effects of the constituents in the pore space on the macroscopic behavior of the porous material. The Biot coefficient is defined as:

$$b = 1 - \frac{\tilde{K}}{\tilde{K}_s} \leq 1 \tag{18}$$

with $\tilde{K}$ the bulk modulus of the porous material (solid matrix and pore space) and $\tilde{K}_s$ the bulk modulus of the solid matrix.

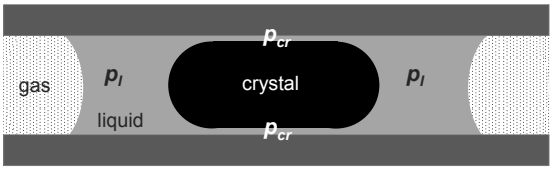

Figure 1: Schematic illustration of a crystal in a pore. A liquid film is maintained between the crystal surface and the pore wall.

The solid pressure is defined using the theory of poromechanics [9, 10]:

$$p_s = \sum_j \left[S_j \left(p_j - p_{0,j} \right) \right] \tag{19}$$

where j represents the different phases present in the pore space, being gas, liquid and crystal. p_j is the pressure exerted by phase j and $p_{0,j}$ is the pressure which accounts for the averaged pressure shift induced by the interface stress, $2\sigma_{s,j}/r$, between the phase and the solid matrix, with respect to the possible values of the pore radius r. The pressure $p_{0,j}$ is expressed as [10]:

$$p_{0,j} = \frac{1}{S_j} \int_0^\infty \frac{2\sigma_{s,j}}{r} \frac{\mathrm{d}S_j}{\mathrm{d}r} \mathrm{d}r \tag{20}$$

As there is a thin liquid film between the salt crystal and the solid matrix (see Figure 1), there is no direct interface between the salt crystal and the solid matrix. Therefore it is reasonable to omit the interfacial stress between the crystal phase and the solid phase ($p_{0,cr}$) and to consider only the interfacial stress between solid and gas phase and solid and liquid phase, $p_{0,g}$ and $p_{0,l}$, respectively. The solid pressure is then expressed as:

$$p_s = S_g p_g + S_l p_l + S_{cr} p_{cr} - S_g p_{0,g} - \left(S_l + S_{cr} \right) p_{0,l} \tag{21}$$

Using the relationship $S_g + S_l + S_{cr} = 1$ and the definition of capillary pressure, equation 2, and defining the crystallization pressure p_x as the difference between the pressure of the crystal phase and the pressure of the liquid phase $p_x = p_{cr} - p_l$, equation 21 becomes:

$$p_s = p_g + \left(S_l + S_{cr} \right) p_c + S_{cr} p_x - S_g p_{0,g} - \left(S_l + S_{cr} \right) p_{0,l} \tag{22}$$

$p_{0,l}$ is defined as:

$$p_{0,l} = \frac{1}{S_l + S_{cr}} \int_0^\infty \frac{2\sigma_{s,l}}{r} \frac{\mathrm{d}\left(S_l + S_{cr} \right)}{\mathrm{d}r} \mathrm{d}r \tag{23}$$

and $p_{0,g}$ as:

$$\begin{aligned} p_{0,g} &= \frac{1}{S_g} \int_0^\infty \frac{2\sigma_{s,g}}{r} \frac{\mathrm{d}\left(S_g \right)}{\mathrm{d}r} \mathrm{d}r \\ &= -\frac{1}{S_g} \int_0^\infty \frac{2\sigma_{s,g}}{r} \frac{\mathrm{d}\left(S_l + S_{cr} \right)}{\mathrm{d}r} \mathrm{d}r \end{aligned} \tag{24}$$

Knowing that $\frac{2\sigma_{s,l}}{r} - \frac{2\sigma_{s,g}}{r}$ equals the capillary pressure p_c, we can write:

$$p_s = p_g + (S_l + S_{cr})\, p_c + S_{cr} p_x + \int_0^\infty p_c \frac{\mathrm{d}\,(S_l + S_{cr})}{\mathrm{d}r} \mathrm{d}r \quad (25)$$

Starting from a reference state $p_s = 0$ defined by $p_g = p_{atm}$, $p_c = p_{c,ref}$ and $p_x = p_{x,ref}$, and assuming that the gas pressure is constant and equal to the atmospheric pressure, equation 25 becomes (similar to [11]):

$$p_s = \int_{p_{c,ref}}^{p_c} (S_l + S_{cr})\, \mathrm{d}p_c + S_{cr}\,(p_x - p_{x,ref}) \quad (26)$$

The crystallization pressure p_x can be seen as a disjoining pressure, representing the interaction forces between the crystal and the solid surface via the thin film.

The effective stress tensor $\boldsymbol{\sigma}$ is given by:

$$\boldsymbol{\sigma} = \boldsymbol{D}\,(\boldsymbol{\epsilon} - \boldsymbol{\epsilon}_T) \quad (27)$$

where $\boldsymbol{D}$ is the elasticity tensor. $\boldsymbol{\epsilon}$ is the second order strain tensor equal to the symmetric gradient of the displacement field $\mathbf{u}$ under the assumption of small deformations:

$$\boldsymbol{\epsilon} = \nabla^{sym}\mathbf{u} \quad (28)$$

$\boldsymbol{\epsilon}_T$ is the thermal strain tensor, accounting for the thermal expansion or contraction of the porous material:

$$\boldsymbol{\epsilon}_T = \alpha_s \mathbf{I}\,(T - T_{ref}) \quad (29)$$

with α_s the thermal expansion coefficient of the solid material and T_{ref} the reference temperature.

2.4 Salt damage

We consider that the porous material exhibits linear elastic mechanical behavior and that the fracture mode is of the mode I type. This means that the tensile stresses act normal to the plane of the crack. We assume that damage occurs, i.e. that a crack develops, when the j^{th} principal component σ_j of the effective stress tensor, determined from equation 16 using definitions 17 and 27, exceeds the material strength f_t^0. This is expressed by the following criterion:

$$f = \sigma_j - f_t^0 \leqslant 0 \quad (30)$$

If equation 30 is violated at a material point, a crack develops.

3 SIMULATION STUDY: DRYING OF A SAMPLE SATURATED WITH SODIUM CHLORIDE SOLUTION

Drying of a Savonnières limestone sample (10x10x8.5 mm^3) at 45°C, initially saturated with a 5.8 molal sodium chloride solution, has been visualized and quantified using quantitative neutron imaging analysis [5]. The sample was prepared by applying a water and vapor tight membrane on the lateral sides (aluminum tape) in order to create a one-dimensional drying process. Drying occurred in the direction perpendicular to the bedding of Savonnières limestone. A hydrophobic treatment (SILRES BS 280, Wacker) was applied on the upper 3 mm of the sample. Drying could only occur through the hydrophobically treated upper part as the bottom surface was sealed. The hydrophobic treatment was intended to prevent salt efflorescence and induce in-pore crystallization. During the drying, the high spatial resolution neutron radiographs (nominal pixel size of 13.5 μm) indicated considerable deformations after about 100 minutes. These deformations represent the displacements induced by crack formation due to the crystallization of sodium chloride. The cracks resulting from the salt crystallization were characterized using X-ray micro-computed tomography. The experiment revealed that the salt crystals precipitate in the upper region of the sample, mainly in the hydrophobic zone, but below the top surface of the sample. Consequently, cracks form in this zone.

In this section, we simulate the coupled heat-moisture-salt transport and salt crystallization in the studied sample and predict the risk for salt damage. Thus we solve equations 1, 4, 5, 8

and 16 and look when the condition 30 is violated. The correct prediction of the salt damage is found to depend strongly on the crystallization kinetics.

3.1 Material and salt properties

3.1.1 Material properties

The total open porosity Φ of the Savonnières limestone used for the experimental study was determined by vacuum saturation and amounts 26.9%. The density of the limestone equals 1975 kg/m^3. During capillary saturation, only 56% of the pore space gets filled. The capillary active porosity of untreated Savonnières limestone amounts $\Phi_{unt} = 14.9\%$. The other pores are only active in the over-capillary regime. When a hydrophobic treatment is applied, the treatment occupies a fraction of the pore space, defined by the porosity Φ_h. The capillary active pore space reduces to $\Phi_{unt} - \Phi_h$. The porosity of the hydrophobic treatment Φ_h at a certain position x is found by:

$$\Phi_h(x) = \Phi_{unt} - \frac{w_{l,cap}(x)}{\rho_l} \tag{31}$$

with $w_{l,cap}(x)$ the capillary moisture content at the position x, determined from the moisture profile in the capillary saturated sample. When salt crystals are precipitating, they as well reduce the capillary active pore space. The crystals occupy a fraction of the pore space $\Phi_{cr} = \Phi S_{cr}$ and the capillary active pore space reduces to $\Phi_{unt} - \Phi_h - \Phi_{cr}$.

The moisture retention curve of Savonnières limestone, describing the liquid saturation degree S_l in function of capillary pressure, is approximated by a sum of power functions [12, 13]:

$$S_l(p_c) = \sum_{j=1}^{s} l_j (1 + (c_j p_c)^{n_j})^{m_j} \tag{32}$$

with s the number of pore systems, l_j weight factors, and c_j, n_j and m_j model parameters. Parameter m_j can be estimated as [12]:

$$m_j = \frac{1 - n_j}{n_j} \tag{33}$$

For the wetting moisture retention curve in the capillary regime, the parameters are given in Table 1. When the capillary active porosity is reduced by a hydrophobic treatment and/or the presence of salt crystals, the liquid saturation degree is reduced in a simplified way by multiplying with the factor $1 - \frac{\Phi_h}{\Phi_{unt}} - \frac{\Phi_{cr}}{\Phi_{unt}}$.

Table 1: Parameters for the analytical fit of the capillary water retention curve.

	1	2	3
c	8.0×10^{-7}	7.0×10^{-6}	1.3×10^{-4}
n	4.27	1.98	1.85
l	0.135	0.256	0.165

The liquid permeability for pure water K_w of Savonnières limestone in function of capillary pressure was determined from the moisture profiles obtained by neutron imaging during a capillary uptake test, as explained in [14]. The liquid permeability for a salt solution K_l can be calculated from the liquid permeability of pure water K_w as:

$$K_l = K_w \frac{\eta_w}{\rho_w} \frac{\rho_l}{\eta_l} \tag{34}$$

where η is the viscosity. The viscosity of sodium chloride solutions with a concentration between 0 to 6 molal in a temperature range of 20 to 150°C is given in [15]. The density, as function of temperature and concentration, can be calculated following Steiger et al. [16, 17]. The relation expressed by equation 34 was confirmed experimentally in [14]. When the capillary active pore space is reduced by a hydrophobic treatment and/or the presence of salt crystals, the liquid permeability is reduced, similar to the liquid saturation degree, by multiplying with the factor $1 - \frac{\Phi_h}{\Phi_{unt}} - \frac{\Phi_{cr}}{\Phi_{unt}}$.

The vapor permeability δ_v was measured with the 'cup method' following EN ISO 12572:2001 [18]. The nonlinear vapor permeability can be described in function of the vapor pressure p_v as:

$$\delta_v = \delta_{v,air} \cdot \left(a + b \exp\left(c \cdot \frac{p_v}{p_{v,sat}} \right) \right) \tag{35}$$

with a, b and c parameters. The vapor permeability in air $\delta_{v,air}$ is given by Schirmer's equation [19, 20]. For flow perpendicular to the bedding direction of the limestone, the parameters a, b and c amount 0.0109, 8.86×10^{-6} and 8.55, respectively. The tortuosity τ of the stone in the perpendicular direction is 24.4.

The thermal conductivity λ was measured using the heat flow meter method (EN 1946-3:1999, [21]). An average thermal conductivity of 0.99 W/mK was found for dry Savonnières limestone. To incorporate the influence of moisture, the thermal conductivity of water λ_w, multiplied with the volume fraction of water, is added to the dry thermal conductivity:

$$\lambda\left(S_l\right) = \lambda_{dry} + \lambda_w \Phi S_l \tag{36}$$

Values for λ_w are given by [22], e.g. at 20°C λ_w equals 0.6 W/mK . The thermal capacity $c_{p,s}$ of Savonnières limestone is estimated to be 900 J/kgK (www.engineeringtoolbox.com). The thermal expansion coefficient α_s was determined by measuring the thermal dilation in a dynamic mechanical analyser (DMA 7e, Perkin Elmer) during a heating-cooling cycle (125°C - 25°C), an average value of 5.5 μm/mK was obtained.

The E-modulus was measured on samples of 16 cm height and 4 x 4 cm^2 cross section. The samples were subjected to a compression load up to 1/3$^{\text{rd}}$ of their compressive strength. During this compression the deformation was measured using a strain gauge device over a length of 10 cm, and the E-modulus was determined from the load-deformation curve. In the dry state, an average E-modulus of 13.9 GPa is found perpendicular to the bedding direction. When the stone is capillary saturated, the E-modulus perpendicular to the bedding direction reduces to 11.2 GPa. The change of E-modulus with saturation degree can be approximated by:

$$E\left(S_l\right) = E_{wet} + \left(E_{dry} - E_{wet}\right) \exp\left(-p \frac{\Phi}{\Phi_{unt}} S_l\right) \tag{37}$$

with p a parameter. We adopt a value of 36 [23], but remark that this value was determined on calcium silicate board. The function 37 expresses that the E-modulus decreases fast to the E-modulus of the wet state when the stone becomes wet ($S_l > 0$). The same behavior was, for example, observed in [24] on Meule sandstone.

The tensile strength of dry Savonnières limestone was determined from a tensile test on samples of 10 cm height and 3.5 x 3.5 cm^2 cross section. In the direction perpendicular to the bedding, the tensile strength $f^0_{t_{dry}}$ equals 1.8 MPa. The tensile strength of the bulk material in function of liquid saturation degree can be written as:

$$f^0_t\left(S_l\right) = \frac{f^0_{t_{dry}}}{E_{dry}} E\left(S_l\right) \tag{38}$$

assuming the same tensile strain in dry and wet conditions.

The Biot coefficient of Savonnières limestone was not measured experimentally, but estimated from literature data of a similar limestone [25]. The Biot coefficient is 0.77.

3.1.2 Salt properties

The salt diffusion coefficient in the porous material, $\mathbf{D}^l_i$, is given by [26]:

$$\mathbf{D}^l_i = \boldsymbol{\tau}^{-1} D\left(C_i, T\right) \Phi S_l^{p_s} \tag{39}$$

where $D\left(C_i, T\right)$ is the diffusion coefficient in function of concentration and temperature in a non-dilute solution, taken from [27], $\boldsymbol{\tau}$ is the tortuosity and p_s the saturation exponent, taken equal to 1.6 [26].

To estimate the heat of crystallization L_{cr}, the method described by [28] is adopted. The heat capacity $c_{p,cr}$ of sodium chloride crystals is obtained from [22].

The supersaturation U and the water activity a_w are calculated using the Pitzer ion interaction approach as described by [29], thus accounting for the non-ideal behavior of pore solutions. The crystallization pressure p_x is then given by [30]:

$$p_x = \frac{RT}{\bar{V}_{cr}} \ln U \tag{40}$$

with R the universal gas constant, T the temperature and $\bar{V}_{cr}$ the molar volume of the crystal, being 27 cm^3/mole for sodium chloride.

The kinetic growth parameters $K_{m,cr}$ and g_{cr} equal 0.41 kg/m^{3}s [31] and 1 for sodium chloride.

The only parameters that are not determined from literature or experiments are the parameters related to the nucleation kinetics. These are the parameters υ, l and U_{start} in the U_{thr}-function (equation 13). The nucleation kinetics determine, together with the growth kinetics, how fast a certain supersaturation gets consumed and thus how long a certain crystallization pressure is acting on the porous material. Therefore a parameter study is done by performing the simulation using an U_{start} value of 1.5 or 2, a l-value of 1×10^{-4} or 1×10^{-3} m and a υ-value of $10\frac{\Phi}{\Phi_{unt}}$, $100\frac{\Phi}{\Phi_{unt}}$ or $1000\frac{\Phi}{\Phi_{unt}}$, resulting in 12 different cases.

3.2 Initial and boundary conditions

The simulation is performed on a 1-dimensional mesh of length L, where L equals the height of the sample used in the drying experiment, being 8.19 mm. The mesh consists of 100 equidistant elements. The time steps are in the order of 1 to 5 ms in order to assure convergence of the coupled system of equations.

The initial capillary pressure at time $t = 0$ equals -100 Pa for every position in the sample, corresponding to the capillary saturated state. The initial temperature of the sample is equal to 45°C. The initial concentration at every position in the sample equals 5.8 molal. In the initial state, no crystals are present in the sample.

The environment surrounding the sample is described by its relative humidity and temperature measured in the experimental drying setup. The relative humidity RH_{env} is 5% and the temperature T_{env} 45°C. Boundary conditions of the Neumann type are imposed on the top surface of the sample, being:

$$\begin{aligned}\bar{q}_m =& CMTC(p_{v,env} - p_{v,surf}) \\ &\text{with } p_{v,env} = p_{v,sat}\left(T_{env}\right) \cdot RH_{env}\end{aligned} \tag{41}$$

$$\begin{aligned}\bar{q}_e =& HTC\left(T_{env} - T_{surf}\right) \\ &+ \left(c_{p,v}\left(T_{surf} - T_0\right) + L_v\right) \cdot \bar{q}_m\end{aligned} \tag{42}$$

with $\bar{q}_m$ the moisture flow and $\bar{q}_e$ the heat flow at the boundary. $p_{v,surf}$ and T_{surf} are the vapor pressure and the temperature at the boundary surface. The convective moisture transfer coefficient $CMTC$ is determined based on a best fitting procedure [5] and amounts 3.95×10^{-9} s/m. The convective heat transfer coefficient $CHTC$ is then given by the Chilton-Colburn analogy [32] and amounts 0.57 W/m^{2}K. The radiative heat transfer coefficient $RHTC$ is 5.1 W/m^{2}K [33] and the total heat transfer coefficient HTC is 5.67 W/m^{2}K. Zero flow boundary conditions are applied on the bottom side of the sample.

3.3 Simulation results

From the experimental results, we know that the sample starts to deform considerably after 100 minutes, representing the displacement induced by crack formation. Thus we expect that the effective stress at a certain position in the sample exceeds the tensile strength around this time. An overview of the effective stress reached after 2.5 hours of drying is given in Table 2 using different values for the nucleation parameters U_{start}, l and υ. Only four of the twelve sets of parameters predict damage within the simulated time frame. The table indicates that the more crystals can spread within the sample (larger l value) and the faster the U_{thr}-function reduces to 1 (larger υ value), the longer it takes before the effective stress exceeds the tensile strength.

We will further discuss one simulation result more in detail. We select the U_{start}-value of 1.5, which corresponds to a concentration increase of 9% by mass with respect to the saturated concentration, close to the maximal value of 10% mentioned by [34]. We look at the simulation result using $l = 1 \times 10^{-4}$ and $\upsilon = 100$, that results in damage after 114 minutes, similar to the experimental result. The effective stress and the strain evolution with time is given by the profiles in Figure 2 and 3b.

Table 2: Maximal effective stress $\sigma_{I,max}$ after 2.5 hours using different nucleation parameters, the height at which this effective stress is reached in the sample, and the time at which cracking occurs if the effective stress exceeds the tensile strength. The '-' symbol indicates that no cracks formed during the first 2.5 hours. The simulation indicated in bold is discussed in detail.

U_{start}	l	υ	$\sigma_{I,max}$	height	time to crack
	m		Mpa	mm	min.
1.5	1×10^{-3}	10	1.03	7.78	-
1.5	1×10^{-3}	100	0.42	7.86	-
1.5	1×10^{-3}	1000	0.41	7.86	-
1.5	1×10^{-4}	10	$> f_t^0$	7.86	89
1.5	$\mathbf{1\times10^{-4}}$	**100**	$\boldsymbol{> f_t^0}$	**7.78**	**114**
1.5	1×10^{-4}	1000	1.06	7.62	-
2.0	1×10^{-3}	10	1.48	7.86	-
2.0	1×10^{-3}	100	0.31	7.86	-
2.0	1×10^{-3}	1000	0.28	7.86	-
2.0	1×10^{-4}	10	$> f_t^0$	7.86	113
2.0	1×10^{-4}	100	$> f_t^0$	7.86	115
2.0	1×10^{-4}	1000	0.95	7.62	-

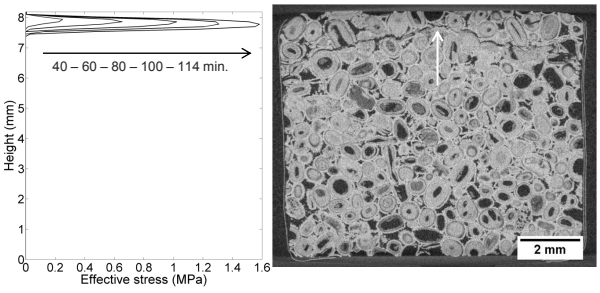

Figure 2: Comparison between the effective stress evolution and the experimentally observed crack pattern. Cracks are observed at the position where the maximal effective stress develops in the simulation.

We observe that the highest effective stresses and strains develop at about 0.4 mm from the top surface of the sample. This is in agreement with the observed crack pattern. A vertical slice obtained from the X-ray tomographic dataset of the sample is shown in Figure 2. A crack developed at the same height as where the effective stress reaches the tensile strenght of 1.58 MPa.

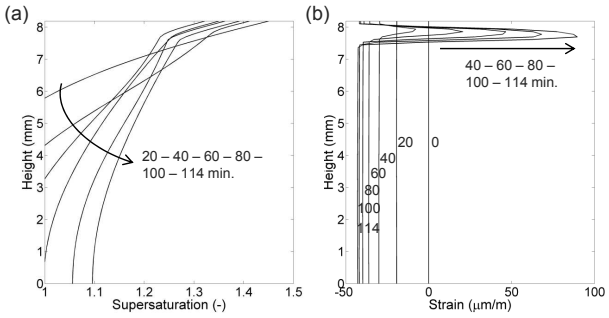

Figure 3: (a) Supersaturation degree and (b) strain evolution.

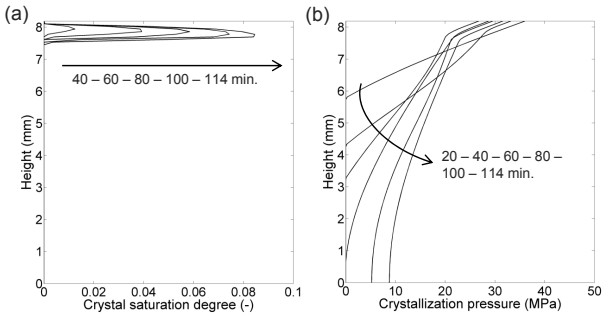

Figure 4: Evolution of (a) the crystal saturation degree and (b) the crystallization pressure.

The effective stress is directly related to the crystal saturation degree S_{cr} and the crystallization pressure p_x. The profiles of these two quantities are given in Figure 4. The product of these two quantities determines the effective stress, as expressed by equation 17. As our sample can deform freely, the solid stress $\boldsymbol{\sigma}_s$ approximates zero. This means that the effective stress $\boldsymbol{\sigma}$ is only determined by the solid pressure p_s. Using equation 26 and considering that our simulation is 1D, so that we can denote the stresses by a scalar (i.e. we describe the stress in the x-direction only), results in:

$$\sigma = b\left(\int_{-100}^{p_c}\left(S_l + S_{cr}\right)\mathrm{d}p_c + S_{cr}p_x\right) \quad (43)$$

The effect of the hygric stresses, expressed by the first term in equation 43 is found to be negligible in this simulation, as they only range in the order of magnitude of 1000 Pa. Thus the effective stress is approximately given by:

$$\sigma \approx bS_{cr}p_x \quad (44)$$

The developed crystallization pressures are directly related to the supersaturation evolution, given in Figure 3a. The U_{start}-value of 1.5 is reached after 23 minutes, from then on, crystals start to form.

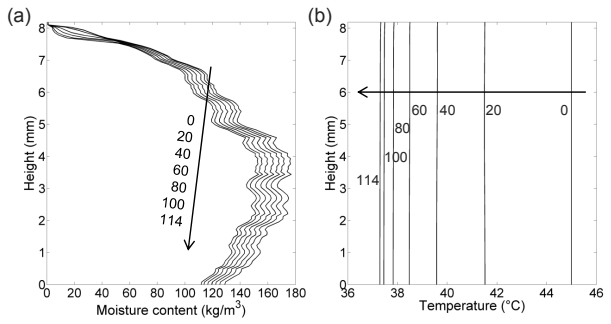

Figure 5: Evolution of (a) the moisture content and (b) the temperature.

The strains in Figures 3b are related to the temperature change in the sample and to the crystal formation. The sample cools down due to evaporative cooling as represented in the profiles of Figure 5b. The cooling causes shrinkage of the sample. As the sample can deform freely and the cooling is uniform over the sample, the strains due to the cooling are uniform and no internal stresses develop due to the thermal shrinkage. When crystals start to form, they cause expansion of the sample in the zone where the crystals precipitate. The moisture content profiles, representing the mass of liquid present in the sample, are given in Figure 5a. The liquid weight decrease is given in Figure 6. The simulation approaches the experimentally obtained data.

The obtained simulation results indicate that we need to consider both the crystallization pressure and the salt crystal distribution to assess damage caused by salt crystallization correctly. The product of these two quantities determines the effective stresses in the porous material. The nucleation and growth kinetics of the salt crystals influence the developed effective stress significantly (see Table 2). This indicates that if you can control the kinetics of crystallization, you can control salt damage.

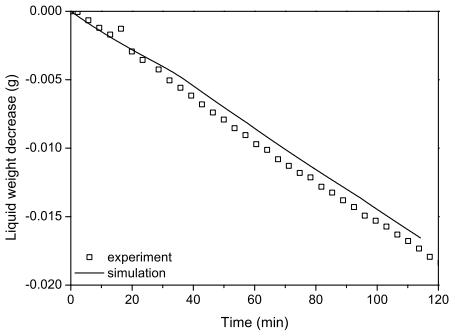

Figure 6: Cumulative liquid weight decrease.

4 CONCLUSIONS

We have developed a fully coupled numerical model that describes heat, water and salt transport, salt crystallization and deformations and damage induced by hygro-thermal and crystallization stresses. The model predicts the macroscopic behavior and physical degradation of porous materials. The model performance is illustrated by the prediction of salt damage caused by the formation of sodium chloride crystals in a porous limestone during drying. The simulation results show a good agreement with the experimental data obtained with neutron and X-ray imaging techniques. The results suggest that controlling the nucleation and growth kinetics is the key factor to control crystallization damage.

REFERENCES

[1] P. Moonen, J. Carmeliet, and L. Sluys, "A continuous-discontinuous approach to simulate fracture processes in quasi-brittle materials," *Philosophical Magazine*, vol. 88, pp. 3281–3298, 2008.

[2] P. Moonen, *Continuous-discontinuous modeling of hygrothermal damage processes in porous media*. PhD thesis, T.U.Delft, The Netherlands & K.U.Leuven, Belgium, 2009.

[3] P. Moonen, L. J. Sluys, and J. Carmeliet, "A continuous-discontinuous approach to simulate physical degradation processes in porous media," *International Journal*

for Numerical Methods in Engineering, vol. 84, pp. 1009–1037, 2010.

[4] P. Moonen, L. J. Sluys, and J. Carmeliet, "A continuous-discontinuous approach to simulate heat transfer in fractured media," *Transport in Porous Media*, vol. 89, pp. 399–419, 2011.

[5] H. Derluyn, *Salt transport and crystallization in porous limestone: neutron - X-ray imaging and poromechanical modeling*. PhD thesis, ETH Zurich, Switzerland, 2012.

[6] H. Derluyn, R. M. Espinosa-Marzal, P. Moonen, and J. Carmeliet, "A coupled transport-crystallization FE model for porous media," in *EURO-C 2010 (Computational modeling of concrete structures)* (N. Bicanic, R. de Borst, H. Mang, and G. Meschke, eds.), (Rohrmoos-Schladming, Austria), pp. 471–479, CRC Press, Taylor & Francis Group, London, UK, 2010.

[7] R. Espinosa, L. Franke, and G. Deckelmann, "Phase changes of salts in porous materials: Crystallization, hydration and deliquescence," *Construction and Building Materials*, vol. 22, pp. 1758–1773, 2008.

[8] M. Koniorczyk, "Modelling the phase change of salt dissolved in pore water - Equilibrium and non-equilibrium approach," *Construction and Building Materials*, vol. 24, pp. 1119–1128, 2010.

[9] O. Coussy, *Poromechanics*. Chichester, UK: John Wiley & Sons Ltd., 2004.

[10] O. Coussy, *Mechanics and Physics of Porous Solids*. Chichester, UK: John Wiley & Sons Ltd., 1st ed., 2010.

[11] B. A. Schrefler and D. Gawin, "The effective stress principle: incremental or finite form?," *International Journal for Numerical and Analytical Methods in Geomechanics*, vol. 20, pp. 785–814, 1996.

[12] M. T. van Genuchten, "A closed-form equation for predicting the hydraulic conductivity of unsaturated soils," *Soil Science Society of America Journal*, vol. 44, pp. 892–898, 1980.

[13] W. Durner, "Hydraulic conductivity estimation for soils with heterogeneous pore structure," *Water Resources Research*, vol. 30, no. 2, pp. 211–223, 1994.

[14] H. Derluyn, M. Griffa, D. Mannes, I. Jerjen, J. Dewanckele, P. Vontobel, A. Sheppard, D. Derome, V. Cnudde, E. Lehmann, and J. Carmeliet, "Characterizing saline uptake and salt profiles in porous limestone with neutron radiography and X-ray micro-tomography," *Journal of Building Physics*, under review.

[15] J. Kestin, H. Ezzat Khalifa, and R. J. Correia, "Tables of the dynamic and kinematic viscosity of aqueous NaCl solutions in the temperature range 20-150 C and the pressure range 0.1-35 MPa," *Journal of Physical and Chemical Reference Data*, vol. 10, no. 1, pp. 71–87, 1981.

[16] M. Steiger, "Chapter 6: Total volumes of crystalline solids and salt solutions," in *An expert chemical model for determining the environmental conditions needed to prevent salt damage in porous materials* (C. Price, ed.), pp. 53–63, 2000.

[17] M. Steiger, "Personal communication," 2008.

[18] CEN, "EN ISO 12572:2001 Hygrothermal performance of building materials and products - Determination of water vapour transmission properties," tech. rep., CEN, 2001.

[19] R. Schirmer, "Die Diffusionszahl von Wasserdampf-Luftgemischen und die

Verdampfungs-geschwindigkeit," *ZVDI Beheift Verfahrenstechnik*, vol. 6, p. 170, 1938.

[20] F. Ochs, W. Heidemann, and H. Mullersteinhagen, "Effective thermal conductivity of moistened insulation materials as a function of temperature," *International Journal of Heat and Mass Transfer*, vol. 51, pp. 539–552, 2008.

[21] SIA, "EN 1946-3:1999 Wärmetechnisches Verhalten von Bauprodukten und Bauteilen - Technische Kriterien zur Begutachtung von Laboratorien bei der Durchführung der Messungen von Wärmeübertragungseigenschaften - Teil 3: Messung nach dem Verfahren mit dem Wärmestrom," tech. rep., SIA Zürich, Zürich, Switzerland, 1999.

[22] W. Haynes and D. Lide, eds., *CRC Handbook of Chemistry and Physics*. Internet Version 2012, 92 ed., 2012.

[23] A. Poupeleer, *Transport and crystallization of dissolved salts in cracked porous building materials*. PhD thesis, K.U.Leuven, Belgium, 2007.

[24] K. E.-A. Van Den Abeele, J. Carmeliet, P. A. Johnson, and B. Zinszner, "Influence of water saturation on the nonlinear elastic mesoscopic response in Earth materials and the implications to the mechanism of nonlinearity," *Journal of Geophysical Research*, vol. 107, p. 2121, 2002.

[25] M. Lion, F. Skoczylas, and B. Ledésert, "Determination of the main hydraulic and poro-elastic properties of a limestone from Bourgogne, France," *International Journal of Rock Mechanics and Mining Sciences*, vol. 41, pp. 915–925, 2004.

[26] A. Buchwald, "Determination of the ion diffusion coefficient in moisture and salt loaded masonry materials by impedance spectroscopy," in *3rd International PhD Symposium*, vol. 2, (Vienna), pp. 475–482, 2000.

[27] J. A. Rard and D. G. Miller, "The mutual diffusion coefficients of Na2SO4-H2O and MgSO4-H2O at 25 C from Rayleigh interferometry," *Journal of Solution Chemistry*, vol. 8, no. 10, pp. 755–766, 1979.

[28] P. Marliacy, R. Solimando, M. Bouroukba, and L. Schuffenecker, "Thermodynamics of crystallization of sodium sulfate decahydrate in H2O-NaCl-Na2SO4: application to Na2SO4.10H2O-based latent heat storage materials," *Thermochimica Acta*, vol. 344, pp. 85–94, 2000.

[29] M. Steiger, J. Kiekbusch, and A. Nicolai, "An improved model incorporating Pitzer's equations for calculation of thermodynamic properties of pore solutions implemented into an efficient program code," *Construction and Building Materials*, vol. 22, pp. 1841–1850, 2008.

[30] M. Steiger, "Crystal growth in porous materials - I: The crystallization pressure of large crystals," *Journal of Crystal Growth*, vol. 282, pp. 455–469, 2005.

[31] R. M. Espinosa-Marzal, "Personal communication," 2009.

[32] T. Chilton and A. P. Colburn, "Mass transfer (absorption) coefficients. Prediction from data on heat transfer and fluid friction," *Industrial & Engineering Chemistry*, vol. 26, no. 11, pp. 1183–1187, 1934.

[33] CEN, "prEN 15026 Hygrothermal performance of building components and building elements - Assessment of moisture transfer by numerical simulation," tech. rep., CEN, Brussels, Belgium, 2004.

[34] R. Flatt, "Salt damage in porous materials: how high supersaturations are generated," *Journal of Crystal Growth*, vol. 242, pp. 435–454, 2002.